Journal of Computational Physics 308 (2016) 389–410

Contents lists available at ScienceDirect

Journal of Computational Physics

www.elsevier.com/locate/jcp

Computations of two-fluid models based on a simple and robust hybrid primitive variable Riemann solver with AUSMD

Yang-Yao Niu

Department of Aerospace Engineering, Tamkang University, New Taipei City, Taiwan, R.O.C.

ARTICLE INFO

Article history:
Received 28 June 2015
Received in revised form 24 November 2015
Accepted 21 December 2015
Available online 23 December 2015

Keywords:
Primitive variable Riemann solver
AUSMD
Two-fluid model
Multi-phase flows

ABSTRACT

This paper is to continue our previous work in 2008 on solving a two-fluid model for compressible liquid–gas flows. We proposed a pressure–velocity based diffusion term original derived from AUSMD scheme of Wada and Liou in 1997 to enhance its robustness. The proposed AUSMD schemes have been applied to gas and liquid fluids universally to capture fluid discontinuities, such as the fluid interfaces and shock waves, accurately for the Ransom's faucet problem, air–water shock tube problems and 2D shock–water liquid interaction problems. However, the proposed scheme failed at computing liquid–gas interfaces in problems under large ratios of pressure, density and volume of fraction. The numerical instability has been remedied by Chang and Liou in 2007 using the exact Riemann solver to enhance the accuracy and stability of numerical flux across the liquid–gas interface. Here, instead of the exact Riemann solver, we propose a simple AUSMD type primitive variable Riemann solver (PVRS) which can successfully solve 1D stiffened water–air shock tube and 2D shock–gas interaction problems under large ratios of pressure, density and volume of fraction without the expensive cost of tedious computer time. In addition, the proposed approach is shown to deliver a good resolution of the shock-front, rarefaction and cavitation inside the evolution of high-speed droplet impact on the wall.

Introduction

The shocks and bubbles of multi-phase flows are easily observed in engineering applications such as in the cooling system within the nuclear reactor, fuel transport system, underwater cavitation problems and droplet erosion problems [1,2]. The importance of multiphase flows in the industry has attracted researchers to develop several mathematical models to simulate the related physics.

One widely accepted approach to model fluids containing individual particles, droplets or bubbles is the so-called two-fluid model [2–4], in which the time or space ensemble average process is applied to model the continuous and disperse phases. Two sets of Navier–Stokes equations are used to describe both phases of fluids with additional inter-phasic terms for the exchange of momentum and energy between phases. Since each phase has its own velocity and temperature, the two-fluid model allows both mechanical and thermal non-equilibrium to be taken into account. In that respect, it represents a more general model for two-phase flows. However, the most notorious characteristic of the two-fluid model is that it is not in conservation form and is not of hyperbolic function. Thus results in an ill-posed problem. Since there is no weak solution for the two-fluid model, it is difficult to capture the shock wave or the contact discontinuity well. Therefore, additional terms or modeling, such as the interfacial pressure force [5] and virtual mass force [6,7], have to be used to render

E-mail address: yyniu@mail.tku.edu.tw.

http://dx.doi.org/10.1016/j.jcp.2015.12.045
0021-9991/

the system of equations hyperbolic. Even though the system is hyperbolic, it is difficult to derive the analytical form of its eigensystem for the implementation of numerical approaches.

Recently, the two-pressure hyperbolic models [8–16,36] are widely studied, such as the seven-equation model proposed by Baer and Nunziato [8] and Saurel and Abgrall [9] for the study of deflagration-to-detonation transition in reactive granular materials. Niu [10] also applied the seven-equation model on the simulation of gas-particle flows with turbulence effects. To keep the hyperbolicity, Allaire et al. [11] and Murrone and Guillard [12] proposed the five-equation models under the assumption of a single velocity and a single pressure for the interface capturing. In addition, a new formulation of Kapila's five-equation model [13,14] is proposed by his group for inviscid, non-heat-conducting, compressible two-fluid flows with a topological equation. E. Romenski et al. [36] proposed a model for two-phase compressible flow based on extended irreversible thermodynamics principles. An isentropic two-phase flow model proposed earlier and the hyperbolic model for heat transfer. To achieve the sharp resolution of interfaces, Shyue and Xiao [15] modified the term of volume fraction by adjusting hyperbolic tangent interpolation to in solving the six-equation two-fluid model. Recently, Michael Dumbser et al. [37] proposed a new high order accurate centered path-conservative method on unstructured triangular and tetrahedral meshes for the solution of multidimensional non-conservative hyperbolic systems, especially they applied to the two- and three-dimensional Baer–Nunziato equations of compressible multiphase flows.

As we know, the two-fluid model is not in conservative form. The non-conservative formulation can cause the solution to oscillate in the vicinity of the interface under the large disparity in materials' properties; it demonstrates considerable difficulty in numerical simulation. It requires some non-standard discretization method to ensure the exactly capturing of the interface. In addition to interface tracking method [16], such as the level set method [17,18] and volume of fluid method [19] use auxiliary transport function to track the fluid interface. Computations of the two-fluid approaches are mostly replied on approximated type Riemann solvers such as HLL and HLLC Riemann solver [20–22]. For example, Sanada et al. [22] used multicomponent Euler equations with the stiffened equation of state which are computed by a FV-WENO scheme with an HLLC Riemann solver that accurately captures shocks and interfaces. In addition, it is well known that the AUSM$^+$ scheme proposed by Liou [23,24] is accurate as Roe's or Osher's approximate Riemann solvers [25,26] without the cost of field-by-field wave decompositions, which makes it amenable to the two-fluid model since its eigensystem is difficult to be expressed in analytical form. Niu [10] first extended the AUSM-family scheme to solve the multiphase flows based on a seven-equation model. It was found that the non-conservative transport equation can easily cause unwanted numerical errors around interfaces. Subsequently, the first successful work was performed by Paillère et al. [27] on the six-equation two-fluid model using modified the AUSM$^+$ scheme. Meanwhile, Edwards et al. [28] extended the AUSM$^+$ scheme to solve a homogeneous mixture model. The extension utilizes the dissipation terms in the AUSMD scheme [24] to enhance its stability in low Mach number flow calculations. The scheme is finally evaluated as AUSM$^+$-up scheme with the extra velocity and pressure dissipation terms [28]. Concurrently, Chang and Liou [29,30] proposed the AUSM$^+$-up scheme combining with the exact Riemann solver to solve the stratified flow model suggested by Stewart and Wendroff [2]. Their approach demonstrates robustness and high-order accuracy in their numerical cases. However, the exact Riemann solver requires tremendous iterations with expensive CPU time consuming. Subsequently, our study demonstrated that the resolution of the fluid interface and pressure waves within liquid phase can be enhanced by adding some extra pressure–density ratio term to the AUSMD [31] for the computations of the fluid interfaces and shock waves, accurately for the Ransom's faucet problem, air–water shock tube problems and 2D shock–water liquid interaction problems. But the AUSMD proposed by [31] failed at computing at computing liquid–gas interfaces under the problems with large ratios of pressure, density and volume of fraction such as the strong shock–gas bubble interaction problems.

In this study, we would propose a hybrid AUSMD type primitive variable Riemann solver (PVRS) to compute numerical fluxes across the gas–gas, liquid–liquid and gas–liquid interfaces universally. It is expected that the new scheme can be efficient, robust as the AUSM type family with the exact Riemann solver. Several benchmark test problems, including the Ransom's faucet problem [32], 1D air–water shock tube problems, a 2D shock–gas bubble and high-speed water droplet impact wall problems would be chosen for numerical validations.

Numerical models

In this section, the system equations of the two-fluid model are described. The related spatial and time discretization of the model equations solved by the approximated Riemann scheme is also introduced. Detailed discussion on how to utilize the stratified flow method can be found in Chang and Liou [29] and Niu et al. [31]. The governing equations of the two-fluid model within the control volume can be written as

$$\Omega \frac{\partial U}{\partial t} + \sum (E)_m n_m S_m - \Omega \boldsymbol{S}^{\text{int}} = 0. \tag{1}$$

First, the so-called "isentropic four-equation model" consists of a mass and a momentum balance equations for each phase is considered. It can be cast in the form (1) with the following definitions:

$$\boldsymbol{U} = \begin{pmatrix} \alpha_g \rho_g \\ \alpha_l \rho_l \\ \alpha_g \rho_g u_g \\ \alpha_l \rho_l u_l \end{pmatrix},$$

$$\boldsymbol{E} = \begin{pmatrix} \alpha_g \rho_g u_g \\ \alpha_l \rho_l u_l \\ \alpha_g \rho_g u_g^2 + \alpha_g p \\ \alpha_l \rho_l u_l^2 + \alpha_l p \end{pmatrix},$$

$$\boldsymbol{S}^{\text{int}} = \begin{pmatrix} 0 \\ 0 \\ g n_m \alpha_g \rho_g + p^{\text{int}} \nabla \alpha_g \\ g n_m \alpha_l \rho_l + p^{\text{int}} \nabla \alpha_l \end{pmatrix},$$

where Ω is the cell volume, t is the physical time step, n_m is an outward-pointing normal vector to face m, and S_m is the area of face m. The conservative variable vectors U, the inviscid fluxes E and the source flux H is the source term containing all the non-differential terms of gravity. The subscripts g and l represent the gas phase and liquid phase; individually. α stands for the phase volume fraction with $\alpha_g + \alpha_l = 1$ and ρ, u, density and velocity for each phase, respectively. And p^{int} is the interfacial pressure [5] given by

$$p^{\text{int}} = p - \sigma \frac{\alpha_g \rho_g \alpha_l \rho_l}{\alpha_g \rho_l + \alpha_l \rho_g} (u_g - u_l)^2, \tag{2}$$

with σ a positive constant. Taking $\sigma \geq 1$ makes the system equations to be hyperbolic and well-posed when the constant $\sigma \geq 1$ as suggested by Stuhmiller [5] for low-speed flows. Recently, the work of Chang et al. [28] pointed out the necessary conditions for hyperbolic system for high speed flow under some extreme conditions is p^{int} larger than the surrounding pressures, thereby resulting in a significant departure from the original problem. Hence, an additional limit on the pressure correction terms is imposed as $p^{\text{int}} = \min(p^{\text{int}}, \varepsilon p)$. In our practice, we usually set $\varepsilon = 0.01$, which has been found sufficient to keep the simulation well behaved. Several runs were conducted to investigate the effects on the solution due to ε for some computationally-challenging problems, e.g., shock–droplet problem; no noticeable effects were found for it varying from 0.001 to 0.1. In this study, it is noted that $\sigma = 2$ is adequate for most of test cases. There has been a vocal community pointing at the ill-posedness of the two-fluid model in its commonly used form, some notable examples being Stewart and Wendroff [2]. Nonetheless, there exists some controversy about the topic, but what is done in current test cases is assuming that the multiple solutions are close enough to each other to introduce only a small uncertainty.

In the four-equation model [27], the system is closed by equation of state for gas and liquid phases. We assume that the gas phase is governed by the isentropic perfect gas equation of state and the liquid phase is governed by Tait's equation of state.

For the gas phase,

$$p = p(\rho_g) = C \left(\frac{\rho_g}{\rho_g^0} \right)^{\gamma}. \tag{3}$$

Here, the parameters used for specifying the thermodynamic properties of vapor are $C = 10^5$ Pa, $\rho_g^0 = 1$ kg/m^3, $\gamma = 1.4$ and the speed of sound is

$$a_g = \sqrt{\frac{\gamma p}{\rho_g}}. \tag{4}$$

For the water, the proposed by Tait's EOS is adopted as

$$p = p(\rho_l) = B \left[\left(\frac{\rho_l}{\rho_l^0} \right)^n - 1 \right], \tag{5}$$

and the speed of sound is

$$a_l = \sqrt{\frac{n}{\rho_l}(p + B)}, \tag{6}$$

with the following constants $n = 7.15$, $B = 3.3 \times 10^8$ Pa, $\rho_l^0 = 1000$ kg/m^3 chosen as being represented of water. From a point of view, the vector of conservative variables U is not a convenient state vector to work with. Indeed, initial and boundary conditions are more often than not specified in terms of primitive variables, such as pressure. Furthermore, from a numerical point of view, and especially in the case of the Riemann solver, primitive variables play a major role in the splitting and discretization of the fluxes. In the case of the four-equation isentropic model, we therefore consider as primitive variables the vector V defined as:

$$V = \begin{pmatrix} \alpha_g \\ u_g \\ u_l \\ p \end{pmatrix}.$$

The transformation matrix between the vectors of the primitive and conservative variables can be expressed as $V = \phi(U)$ based on

$$U = \begin{pmatrix} \alpha_g \rho_g \\ \alpha_l \rho_l \\ \alpha_g \rho_g u_g \\ \alpha_l \rho_l u_l \end{pmatrix}.$$

After solving the non-linear system equation $V - \phi(U) = 0$, we can have

$$u_g = \frac{U_3}{U_1}, \qquad u_l = \frac{U_4}{U_2},$$

with

$$\alpha \rho_g(p) = U_1, \tag{7}$$

and

$$(1-\alpha)\rho_1(p) = U_2. \tag{8}$$

To achieve the common pressure between different phases, we can substitute (7) into (8) to eliminating α; also substituting into Equations (2) and (4), a non-linear equation is achieved as

$$F(p) = \left\{ \left[1 - \frac{u_1}{\rho_g^0 (\frac{p}{C})^{\frac{1}{\gamma}}} \right] \left[\left(\frac{p}{B} + 1 \right) \right] \right\} = 0, \tag{9}$$

and the first derivatives of $F(p)$ with respect to p is

$$F'(p) = \rho_l^0 \left\{ \frac{u_1}{C\gamma\rho_g^0} \left(\frac{p}{C} \right)^{-\frac{1}{\gamma}-1} \left[\left(\frac{p}{B} \right) + 1 \right]^{\frac{1}{n}} + \frac{1}{nB} \left[1 - \frac{u_1}{\rho_g^0 (\frac{p}{C})^{\frac{1}{\gamma}}} \right] \left[\frac{p}{B} + 1 \right]^{\frac{1}{n}-1} \right\}. \tag{10}$$

The pressure can be easily obtained by solving the function $F(p)$ defined over the real pressure, and its derivative $F'(p)$ with few iterations in each time step based on the Newton–Raphson iteration method.

Secondly, the six-equation model [27] consisting of mass, a momentum and energy balance equations for each phase is considered. It can be cast in the form (1) with the following definitions:

$$U = \begin{bmatrix} \alpha_g \rho_g \\ \alpha_l \rho_l \\ \alpha_g \rho_g u_g \\ \alpha_l \rho_l u_l \\ \alpha_g \rho_g E_g \\ \alpha_l \rho_l E_l \end{bmatrix}, \qquad E = \begin{bmatrix} \alpha_g \rho_g u_g \\ \alpha_l \rho_l u_l \\ \alpha_g \rho_g u_g^2 + \alpha_g p \\ \alpha_l \rho_l u_l^2 + \alpha_l p \\ \alpha_g \rho_g u_g H_g \\ \alpha_l \rho_l u_l H_l \end{bmatrix} \quad \text{and} \quad \boldsymbol{S}^{\text{int}} = \begin{bmatrix} 0 \\ 0 \\ g_x \alpha_g \rho_g + p^{\text{int}} \nabla \alpha_g \\ g_x \alpha_l \rho_l + p^{\text{int}} \nabla \alpha_l \\ -p^{\text{int}} \frac{\partial \alpha_g}{\partial t} + g_x \alpha_g \rho_g u_g \\ -p^{\text{int}} \frac{\partial \alpha_l}{\partial t} + g_x \alpha_l \rho_l u_l \end{bmatrix}.$$

The total energy $E_k = e_k + \frac{1}{2}u_k^2$ where e is denoted by the internal energy. The enthalpy $H = E + p/\rho$. Here, we neglect viscous terms, also assume that no phase change occurs between the air and liquid phases. In this work, the system equations are required to close by equations of states and the gas and liquid fluids are governed by the perfect gas and stiffened gas model, respectively.

Equation of state

For the gas phase,

$$P_g = \rho_g R_g T_g, \qquad e_g = \frac{R_g}{\gamma_g - 1} T_g. \tag{12}$$

Here, the parameters used for specifying the thermodynamic properties of vapor are

$$\rho_g = 1\ \text{kg/m}^3, \qquad \gamma_g = 1.4, \qquad R_g = 288.2\ \frac{\text{J}}{\text{kg K}},$$

and the speed of sound is

$$a_g = \left(\frac{\gamma_g P}{\rho_g} \right)^{1/2}. \tag{13}$$

For the water, the stiffened gas model proposed by Harlow and Amsden [2] is adopted as:

$$p_l = \frac{\gamma_l - 1}{\gamma_l}\rho_l C_{pl} T_l - p_\infty, \qquad e_l = \frac{C_{pl}}{\gamma_l} T_l + \frac{p_\infty}{\rho_l}, \tag{14}$$

and the speed of sound is

$$a_l = \left(\frac{\gamma_l (p_l + p_\infty)}{\rho_l}\right)^{1/2}. \tag{15}$$

Here, the parameters used for specifying the thermodynamic properties of water are determined to meet the following criteria. When $T_l = 293.15$ K and $P = 1.0132 \times 10^5$ Pa, we set the following properties based on data:

$$\gamma_l = 1.932, \qquad C_{pl} = 8095.08 \ \frac{\mathrm{J}}{\mathrm{kg\,K}}, \qquad p_\infty = 1.1645 \times 10^9 \ \mathrm{Pa}.$$

Please note that the existence of the huge constant p_∞ represents a very weak link between pressure and density function. The density will keep almost unchanged even when a very big pressure is applied. Therefore, how to enhance the coupling between pressure and density field is a key point to achieve accurate modeling of low-speed compressible liquid flow. Before performing numerical flux calculations, we need to know the primitive variable as

$$V = \begin{bmatrix} \alpha_g \\ u_g \\ u_l \\ p \\ T_g \\ T_l \end{bmatrix}.$$

The transformation matrix between the vectors of the primitive variable and conservative variable can be expressed by $V = \phi(U)$ based on

$$U = \begin{bmatrix} \alpha_g \rho_g \\ \alpha_l \rho_l \\ \alpha_g \rho_g u_g \\ \alpha_l \rho_l u_l \\ \alpha_g \rho_g E_g \\ \alpha_l \rho_l E_l \end{bmatrix}.$$

After solving the non-linear system $V - \phi(U) = 0$, we can have

$$u_g = \frac{U_3}{U_1}, \qquad u_l = \frac{U_4}{U_2}, \qquad e_g = \frac{U_5}{U_1} - \frac{1}{2}\left(\frac{U_3}{U_1}\right)^2 \quad \text{and} \quad e_l = \frac{U_6}{U_2} - \frac{1}{2}\left(\frac{U_4}{U_1}\right)^2, \tag{16}$$

with

$$U_1 = \alpha_g \rho_g(p, T), \tag{17}$$

and

$$U_2 = (1 - \alpha_g)\rho_l(p, T). \tag{18}$$

To achieve the common pressure between different phases, we can substitute (17) into (18) to eliminate α_g also substituting into equation (12) and equation (14), a non-linear equation $F(p) = 0$ is achieved as

$$p^2 + \left[\gamma_l p_\infty - U_1(\gamma_g - 1)e_g - U_2 p(\gamma_l - 1)e_l\right]p - U_1(\gamma_g - 1)e_g \gamma_l p_\infty = 0. \tag{19}$$

The pressure can be easily obtained by solving equation (13) based on the Newton–Raphson iteration method. Then the volume fractions of both phases can be achieved after the pressure is known as

$$\alpha_g = \frac{U_1(\gamma_g - 1)e_g}{p}, \tag{20}$$

and

$$\alpha_l = 1 - \alpha_g. \tag{21}$$

Also, the density of each phase can be achieved differently as

$$\rho_g = \frac{U_1}{\alpha_g}, \tag{22}$$

and

$$\rho_l = \frac{U_2}{\alpha_l}. \tag{23}$$

Finally, the temperature of each phase can be computed as

$$T_g = \frac{\gamma_g - 1}{R_g} e_g, \tag{24}$$

and

$$T_l = \frac{\gamma_l e_l (p + p_\infty)}{C_p (p + \gamma_l p_\infty)}, \text{ respectively.} \tag{25}$$

Spatial and time discretization

For the spatial discretization, the primitive variables on cell interface are determined through the second- or third-order spatial accurate Chakravarthy type MUSCL approach shown in [33] working for compressing volume fractions on non-uniform and uniform grids. In this paper, it is found that there is no noticeable difference between solutions obtained from second- or third-order schemes. Only results done by the interpolation with the third-order spatial accuracy are presented. Once the primitive variables on the left and right of the cell interface are determined, here, we use a primitive variable Riemann solver in the AUSMD form to calculate the numerical fluxes across the interface. As we know, the basic ideal for the AUSM$^+$ scheme is to split the numerical flux into the convection flux and pressure flux. Then one of the choices is using flux difference to evaluate the mass flux of the convection flux, and for the pressure flux, respectively. Here, the well-known interface convective numerical flux of AUSMD can be divided in the convective flux and pressure flux defined as

$$E_{1/2} = \frac{1}{2}\big[(a_{1/2} m_{1/2} \rho_{L/R} + D_p)_{1/2} (\Psi_L + \Psi_R) - a_{1/2} \big| (a_{1/2} m_{1/2} \rho_{L/R} + D_p) \big| (\Psi_R - \Psi_l)\big] + P_{1/2}, \tag{26}$$

where

$$\Psi = \begin{pmatrix} 1 \\ u \\ H \end{pmatrix} \quad \text{and} \quad P_{1/2} = \begin{pmatrix} 0 \\ p + D_u \\ 0 \end{pmatrix}.$$

The subscript "L/R" means the variables are chosen in an upwind manner. For example, if $m_{1/2} \geq 0$, then $\rho_{L/R} = \rho_L$; otherwise $\rho_{L/R} = \rho_R$. The $a_{1/2}$ is the mean speed of sound. Here we simply use simple average:

$$a_{\frac{1}{2}} = \frac{1}{2}(a_R + a_L). \tag{27}$$

Then we can define the Mach number for left and right states:

$$M_L = \frac{u_L}{a_{1/2}} \quad \text{and} \quad M_R = \frac{u_R}{a_{1/2}}. \tag{28}$$

The splitting functions $m_{1/2}$ and $p_{1/2}$ are defined as

$$m_{1/2} = \mathsf{M}^+_{(4)}(M_L) + \mathsf{M}^-_{(4)}(M_R), \tag{29}$$

and

$$p_{1/2} = \mathsf{P}^+_{(5)}(M_L) + \mathsf{P}^-_{(5)}(M_R), \tag{30}$$

with

$$\mathsf{M}^\pm_{(4)}(M) = \begin{cases} \pm(M \pm 1)^2 \pm (M^2 - 1)^2, & |M| < 1 \\ \mathsf{M}^\pm_{(1)}(M) & \text{otherwise} \end{cases} \tag{31}$$

$$\mathsf{P}^\pm_{(5)}(M) = \begin{cases} \frac{1}{4}(M \pm 1)^2 (2 \mp M) \pm \frac{3}{16} M (M^2 - 1)^2 & |M| < 1 \\ (1/M)\mathsf{M}^\pm_{(1)}(M) & \text{otherwise,} \end{cases} \tag{32}$$

and

$$\mathsf{M}^\pm_{(1)}(M) = \frac{1}{2}\big(M \pm |M|\big), \tag{33}$$

where the subscript "(1)", "(4)" and "(5)" mean the order of the polynomial of the splitting functions. It is well known that the mass flux of AUSM$^+$-up scheme ("-up" indicates the pressure and velocity based dissipation terms) is usually expressed as

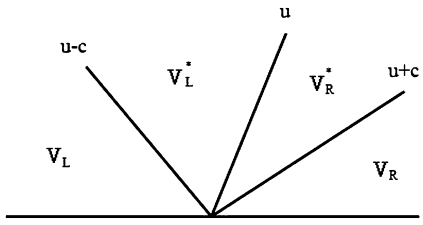

Fig. 1. The structure of the one-dimensional Riemann problem.

(I) The dissipation term in the mass of flux of AUSM$^+$-up scheme is

$$D_p = \kappa_p \frac{\Delta \mathrm{M} \cdot \max(1 - \bar{M}^2, 0) \cdot (p_L - p_R)}{a_{1/2}}, \tag{34}$$

and

$$D_u = \kappa_u \mathrm{P}^+_{(5)}(\bar{M}_L)\mathrm{P}^-_{(5)}(\bar{M}_R)\rho_{1/2} a_{1/2}(u_L - u_R), \tag{35}$$

with

$$\begin{aligned}\Delta \mathrm{M} &= \mathrm{M}^+_{(4)}(M_L) - \mathrm{M}^+_{(1)}(M_L) - \mathrm{M}^-_{(4)}(M_R) + \mathrm{M}^-_{(1)}(M_R) \\ &= \delta \mathrm{M}^+(M_L) - \delta \mathrm{M}^-(M_R),\end{aligned} \tag{36}$$

and

$$\bar{M} = \frac{1}{2}(M_L + M_R). \tag{37}$$

Another choice is in our previous work, we suggest different dissipation terms for D_p and D_u which are designed to imitate the dissipation terms of AUSMD scheme proposed by Wada and Liou [23]. The dissipation terms suggested in [28] are incorporating with time pre-conditioning method, it demonstrated accurate and robust in solving all-speed gas flow problems.

(II) The dissipation term in the mass of flux in AUSMD scheme is

$$D_p = \sqrt{\frac{\rho_L \rho_R}{p_L \rho_R + p_R \rho_L}}\, \Delta M \cdot \max\left(1 - \mathrm{int}\left(\bar{M}^2\right), 0\right) \cdot (p_L - p_R), \tag{38}$$

and

$$D_u = \mathrm{P}^+_{(5)}(M_L)\mathrm{P}^-_{(5)}(M_R)\rho_{1/2} a_{1/2}(u_L - u_R). \tag{39}$$

It shows very good capability to capture pressure wave in either gas or liquid flows. However, both dissipation terms (I) and (II) produced oscillating errors on the computations of the liquid–gas interfaces with large ratios of pressure, density and volume of fraction. Therefore, Chang and Liou [29] suggested using the exact Riemann solver to calculate the numerical fluxes across the gas–liquid interface and it showed very good results in simulating flows with complex shock-interface interactions. The only deficiency of the exact Riemann solver is to require the iterations of pressure in every time step, hence making it very time consuming. In addition to using the exact Riemann solver, we wish to look for a robust and efficient scheme which can be applied on the resolution of the entire gas–gas, liquid–liquid and gas–liquid interface consistently.

To our knowledge, no exact Riemann solver is known in the literature for numerical flux of a general two-fluid model of a real fluid. Chang and Liou employed the stiffened gas EOS with a constant ratio of specific heats, which is only slightly different from the perfect gas EOS. They showed that the exact solution of a Riemann problem for the stiffened gas can be derived quite simply. Since the exact Riemann solver is still more expensive to compute than other approximate solvers, they only used the exact Riemann solver in the vicinity of the fluid interface. Here, we find that an analytic solution of one dimensional Riemann problem can be applied on the mass flux in AUSMD without extra dissipative terms to simulate the numerical flux around the interfaces between same and different phases. We consider a one dimensional Riemann problem as noted in Toro [26].

The computation domain is divided into four regions as shown in Fig. 1 by the waves propagating across the domain. The wave associated with the eigenvalues $(u + a)$ and $(u - a)$ can be either a shock wave or a rarefaction wave, and the wave associated with the eigenvalue u is a contact discontinuity. Then we can assign the flow properties in the four regions respectively. We know the Riemann solution between the given endpoints u_L and u_R, the associated path classically involves two state u^*_L and u^*_R respectively corresponding to the left and right states to the contact discontinuity. We recall that the sup-baths both correspond to genuinely nonlinear fields connecting V^*_L to V^*_R is associated with two linearly degenerate fields. The states p^* and u^* are obtained by solving the following classical system made of Riemann invariants. Note that if the data states V_L and V_R are connected by a single isolated contact discontinuity or shear wave, then the approximate solutions is to solve the characteristic equations as

$$dp - \rho a du = 0 \quad \text{along} \quad dx/dt = u - a, \tag{41}$$

$$dp - a^2 d\rho = 0 \quad \text{along} \quad dx/dt = u, \tag{42}$$

$$dp + \rho a du = 0 \quad \text{along} \quad dx/dt = u + a. \tag{43}$$

These differential relations hold true along the characteristic directions. First we set

$$C = \rho a, \tag{44}$$

then, in order to find the star values, we connect the state V_L to the data state V_L by integrating (43) along the characteristic of speed $u + a$, where C is evaluated at the foot of the characteristic.

$$\bar{p} + C_L \bar{u}_L = p_L + C_L u_L. \tag{45}$$

Similarly, we connect V_L to the data state V_R by integrating (41) along the characteristic of speed $u - a$, with C is evaluated at the foot of the characteristic.

We can obtain

$$\bar{p} - C_R \bar{u}_R = p_R - C_R u_R. \tag{46}$$

The values of star region can be obtained; The complete solution for numerical flux of the liquid–liquid interface and gas–gas interface is

$$\begin{aligned}
\bar{p} &= \frac{1}{C_L + C_R}\left[C_R p_L + C_L p_R + C_L C_R (u_L - u_R)\right], \\
\bar{u} &= \frac{1}{C_L + C_R}\left[C_L u_L + C_R u_R + (p_L - p_R)\right], \\
\bar{\rho}_L &= \rho_L + (\bar{p} - \rho_L)/a_L^2, \\
\bar{\rho}_R &= \rho_R + (\bar{p} - \rho_R)/a_R^2.
\end{aligned} \tag{47}$$

Notice that in this linearized solution we only need to specify constant values for $\bar{\rho}$ and $\bar{a}$. Selecting some average of the data values ρ_L, ρ_R, a_L, a_R appears sensible.

$$\bar{\rho} = \frac{1}{2}(\bar{\rho}_L + \bar{\rho}_R), \qquad \bar{a} = \frac{1}{2}(a_L + a_R). \tag{48}$$

In this approximation, we do not need to make a choice for the averages $\bar{\rho}$ and $\bar{a}$; their values are replaced by data values at the foot of the corresponding characteristics. If $C_L = C_R = \bar{\rho}\bar{a}$, the approximations of (47) for the primitive variables on the gas–gas interface becomes.

$$\begin{aligned}
p^*_{g-g} &= \frac{1}{2}\left[p_L + p_R + \left(u_L^g - u_R^g\right)/\bar{\rho}\bar{a}\right], \\
u^*_{g-g} &= \frac{1}{2}\left[u_L^g + u_R^g + \left(p_L^g - p_R^g\right)/\bar{\rho}\bar{a}\right], \\
\rho^*_{L,g-g} &= \rho_L^g + \left(p^*_{g-g} - p_L^g\right)/a_L^2, \\
\rho^*_{R,g-g} &= \rho_R^g + \left(p^*_{g-g} - p_R^g\right)/a_R^2, \\
\rho^*_{g-g} &= \frac{1}{2}\left(\rho^*_{L,g-g} + \rho^*_{R,g-g}\right).
\end{aligned} \tag{49}$$

And the approximations of (47) for the primitive variables on the liquid–liquid interface becomes.

$$\begin{aligned}
p^*_{l-l} &= \frac{1}{2}\left[p_L^l + p_R^l + \left(u_L^l - u_R^l\right)/\bar{\rho}\bar{a}\right], \\
u^*_{l-l} &= \frac{1}{2}\left[u_L^l + u_R^l + \left(p_L^l - p_R^l\right)/\bar{\rho}\bar{a}\right], \\
\rho^*_{L,l-l} &= \rho_L^l + \left(p^*_{l-l} - p_L^l\right)/a_L^2, \\
\rho^*_{R,l-l} &= \rho_R^l + \left(p^*_{l-l} - p_R^l\right)/a_R^2, \\
\rho^*_{l-l} &= \frac{1}{2}\left(\rho^*_{L,l-l} + \rho^*_{R,l-l}\right).
\end{aligned} \tag{50}$$

For developing numerical flux across the gas–liquid interface, we consider the gas phase on the left region of the material interface and the liquid on the right region, the complete solution of (47) can be

$$
\begin{aligned}
p^*_{g-l} &= \frac{1}{C_L + C_R}\left[C_R p^g_L + C_L p^l_R + C_L C_R\left(u^g_L - u^l_R\right)\right],\\
u^*_{g-l} &= \frac{1}{C_L + C_R}\left[C_L u^g_L + C_R u^l_R + \left(p^g_L - p^l_R\right)\right],\\
\rho^*_{L,g-l} &= \rho^g_L + \left(p^*_{g-l} - p^g_L\right)/a^2_L,\\
\rho^*_{R,g-l} &= \rho^g_R + \left(p^*_{g-l} - p^l_R\right)/a^2_R,\\
\rho^*_{g-l} &= \frac{1}{2}\left(\rho^*_{L,g-l} + \rho^*_{R,g-l}\right),
\end{aligned} \tag{51}
$$

by choosing $C_L = \rho^g_L a^g_L$ and $C_R = \rho^l_R a^l_R$.

For the numerical flux across the liquid phase on the left region of the material interface and the gas phase on the right region, the complete solution of (47) can be

$$
\begin{aligned}
p^*_{l-g} &= \frac{1}{C_L + C_R}\left[C_R p^l_L + C_L p^g_R + C_L C_R\left(u^l_L - u^g_R\right)\right],\\
u^*_{l-g} &= \frac{1}{C_L + C_R}\left[C_L u^l_L + C_R u^g_R + \left(p^l_L - p^g_R\right)\right],\\
\rho^*_{L,l-g} &= \rho^l_L + \left(p^*_{l-g} - p_L\right)/a^2_L,\\
\rho^*_{R,l-g} &= \rho^g_R + \left(p^*_{l-g} - p_R\right)/a^2_R,\\
\rho^*_{l-g} &= \frac{1}{2}\left(\rho^*_{L,l-g} + \rho^*_{R,l-g}\right)
\end{aligned} \tag{52}
$$

by choosing $C_L = \rho^l_L a^l_L$ and $C_R = \rho^g_R a^g_R$.

Finally, the proposed numerical fluxes can be represented respectively as for the gas–gas interface,

$$
E_{g-g} = \frac{1}{2}\left[\left(\rho^*_{g-g}u^*_{g-g}\right)_{1/2}(\Psi_L + \Psi_R) - \left|\left(\rho^*_{g-g}u^*_{g-g}\right)\right|(\Psi_R - \Psi_l)\right] + P_{1/2}, \tag{53}
$$

where

$$
\Psi_L = \begin{pmatrix} 1 \\ u_L \\ H_L \end{pmatrix}, \qquad \Psi_R = \begin{pmatrix} 1 \\ u_R \\ H_R \end{pmatrix} \quad \text{and} \quad P = \begin{pmatrix} 0 \\ p^*_{g-g} \\ 0 \end{pmatrix}.
$$

For the liquid–liquid interface,

$$
E_{l-l} = \frac{1}{2}\left[\left(\rho^*_{l-l}u^*_{l-l}\right)_{1/2}(\Psi_L + \Psi_R) - \left|\left(\left(\rho^*_{l-l}u^*_{l-l}\right)\right)\right|(\Psi_R - \Psi_l)\right] + P_{1/2}, \tag{54}
$$

where

$$
\Psi_L = \begin{pmatrix} 1 \\ u_L \\ H_L \end{pmatrix}, \qquad \Psi_R = \begin{pmatrix} 1 \\ u_R \\ H_R \end{pmatrix} \quad \text{and} \quad P_{1/2} = \begin{pmatrix} 0 \\ p^*_{l-l} \\ 0 \end{pmatrix}.
$$

For the liquid–gas interface,

$$
E_{l-g} = \frac{1}{2}\left[\left(\rho^*_{l-g}u^*_{l-g}\right)_{1/2}(\Psi_L + \Psi_R) - \left|\left(\left(\rho^*_{l-g}u^*_{l-g}\right)\right)\right|(\Psi_R - \Psi_l)\right] + P_{1/2}, \tag{55}
$$

where

$$
\Psi_L = \begin{pmatrix} 1 \\ u_L \\ H_L \end{pmatrix}, \qquad \Psi_R = \begin{pmatrix} 1 \\ u_R \\ H_R \end{pmatrix} \quad \text{and} \quad P_{1/2} = \begin{pmatrix} 0 \\ p^*_{l-g} \\ 0 \end{pmatrix}.
$$

For the gas–liquid interface,

$$
E_{g-l} = \frac{1}{2}\left[\left(\rho^*_{g-l}u^*_{g-l}\right)_{1/2}(\Psi_L + \Psi_R) - \left|\left(\left(\rho^*_{g-l}u^*_{g-l}\right)\right)\right|(\Psi_R - \Psi_l)\right] + P_{1/2}, \tag{56}
$$

where

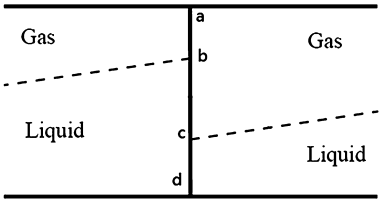

Fig. 2. Discretization based on stratified flow model.

$$\Psi_L = \begin{pmatrix} 1 \\ u_L \\ H_L \end{pmatrix}, \qquad \Psi_R = \begin{pmatrix} 1 \\ u_R \\ H_R \end{pmatrix} \quad \text{and} \quad P_{1/2} = \begin{pmatrix} 0 \\ p^*_{g-l} \\ 0 \end{pmatrix}.$$

The general discretization form of Eq. (1) for each cell Ω_j can be organized as

$$\Omega_j \partial_t \begin{pmatrix} \alpha_k\rho_k \\ \alpha_k\rho_k u_k \\ \alpha_k\rho_k E_k \end{pmatrix}_j + \sum (\overline{ab} E_{g-g} + \overline{bc} E_{l-g} + \overline{bc} E_{g-l} + \overline{cd} E_{l-l})_m n_m S_m + \Omega_j \begin{pmatrix} 0 \\ 0 \\ p^{\text{int}} \partial_t \alpha_k \end{pmatrix}_j - \sum \begin{pmatrix} 0 \\ p_{\text{int}} \alpha_k \\ 0 \end{pmatrix}_m n_m S_m = \Omega_j \begin{pmatrix} 0 \\ \rho_k \alpha_k g \\ \rho_k \alpha_k u_k g \end{pmatrix}_j . \tag{57}$$

Here the subscript $k = g$ or l representing gas phase or liquid phase. The functions $\overline{ab}$, $\overline{bc}$ and $\overline{cd}$ are the effective length of each type of interfaces as shown in Fig. 2. We define

$$\begin{aligned} &\overline{ab} = \min\left(\alpha_g^L, \alpha_g^R\right), \\ &\overline{bc} = \max\left(0, \alpha_l^R - \alpha_g^L\right) \quad \text{or} \\ &\overline{bc} = \max\left(0, \alpha_g^R - \alpha_l^L\right), \\ &\overline{cd} = \min\left(\alpha_l^L, \alpha_l^R\right). \end{aligned} \tag{58}$$

After applying the Runge–Kutta time marching method to perform the time integration. Referring to the general discretization, it can be proceeded as:

$$\begin{aligned} U_k^{(1)} &= Q_k^n - \Delta t L\left(Q^n\right), \\ U_k^{(2)} &= \frac{3}{4} Q_k^n - \frac{1}{4}\left[Q_k^{(1)} - \Delta t L\left(Q_k^{(1)}\right)\right], \\ U_k^{n+1} &= \frac{1}{3} Q_k^n + \frac{2}{3}\left[Q_k^{(2)} - \Delta t L\left(Q_k^{(2)}\right)\right], \end{aligned} \tag{59}$$

where

$$U_k = \begin{pmatrix} \alpha_k\rho_k \\ \alpha_k\rho_k u_k \\ \alpha_k\rho_k E_k + p_{\text{int}}\alpha_k \end{pmatrix},$$

and

$$L(U_k) = -\sum \left(\overline{ab} E_{g-g} + \overline{bc}\left(E_{l-g} - (p_{\text{int}}\alpha_k)_{l-g}\right) + \overline{bc}\left(E_{g-l} - (p_{\text{int}}\alpha_{k\,g-l})\right) + \overline{cd} E_{l-l}\right)_m n_m S_m + \Omega_j \begin{pmatrix} 0 \\ \rho_k\alpha_k g \\ \rho_k\alpha_k u_k g - p_{\text{int}}\alpha_k \end{pmatrix}_j , \tag{60}$$

with $E = E(V^L_{i+1/2}, V^R_{i+1/2})$. The states variables $V^L_{i+1/2,j}$ and $V^R_{i+1/2,j}$ are interpolated from the cell centered states by means of the MUSCL (Monotonic Upstream Schemes for Conservation Laws) type schemes [33]. They can be expressed as

$$V^R_{i+1/2,j} = V_{i+1,j} - a_{i+1,j}\left[(c_{i+1,j} - 2kb_{i+1,j})(V_{i+2,j} - V_{i+1,j}) + \frac{1}{c_{i+1,j}}(1 - 2kb_{i+1,j})(V_{i+1,j} - V_{i,j})\right],$$

and

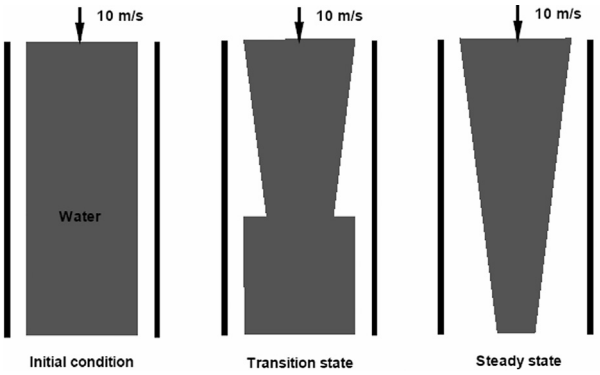

Fig. 3. Illustration of Ransom's water faucet problem.

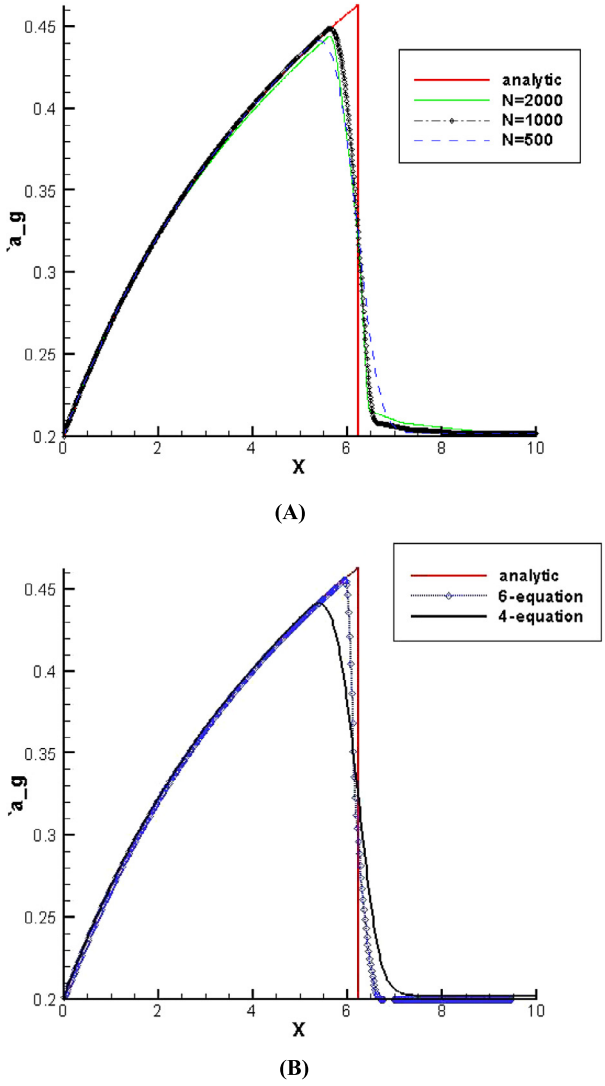

Fig. 4. (A) several different grids by the four-equation model and (B) different approaches are used in the water faucet problem by the four- and six-equation model (500 grid points).

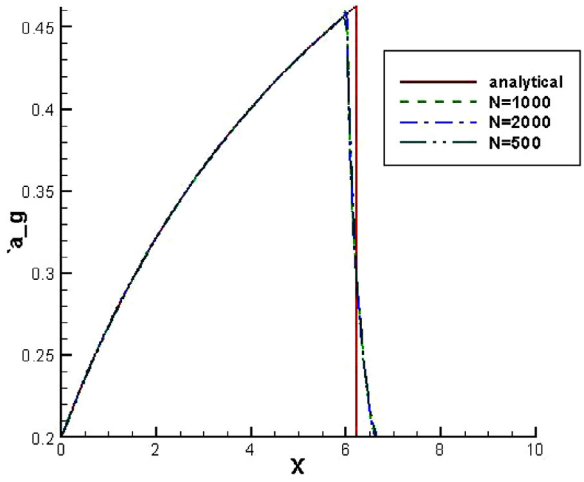

(A)

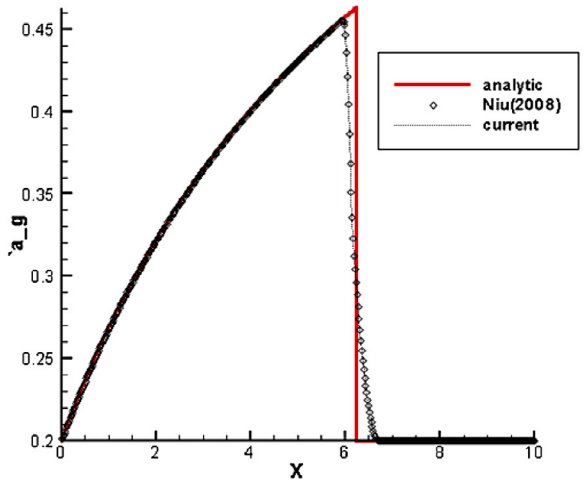

(B)

Fig. 5. (A) several different grids and (B) different approaches are used in the water faucet problem by the six-equation model (500 grid points).

$$V^{L}_{i+1/2,j} = V_{i,j} - a_{i,j}\left[(c_{i,j} - 2kb_{i,j})(V_{i,j} - V_{i-1,j}) + \frac{1}{c_{i,j}}(1 - 2kb_{i,j})(V_{i+1,j} - V_{i,j})\right], \tag{61}$$

where $k = 1/3$ and the non-uniformity of cell sizes is taken into account in $a_{i,j}$, $b_{i,j}$, $c_{i,j}$. Let $l_{i,j}$ represents the width of cell in the i direction; then

$$a_{i,j} = \frac{l_{i,j}}{l_{i+1,j} + 2l_{i,j} + l_{i-1,j}},$$

$$b_{i,j} = \frac{l_{i,j}}{l_{i,j} + l_{i+1,j}},$$

and

$$c_{i,j} = \frac{l_{i,j} + l_{i-1,j}}{l_{i,j} + l_{i+1,j}}.$$

The choice of the physic time step Δt is decided by the local time step determined by the largest eigenvalue of the governing equations for each grid cell by the CFL condition (Courant–Friedrichs–Lewy condition) like

$$\Delta t = \frac{CFL\Delta x}{\max(u_g + a_g, u_l + a_l)}. \tag{62}$$

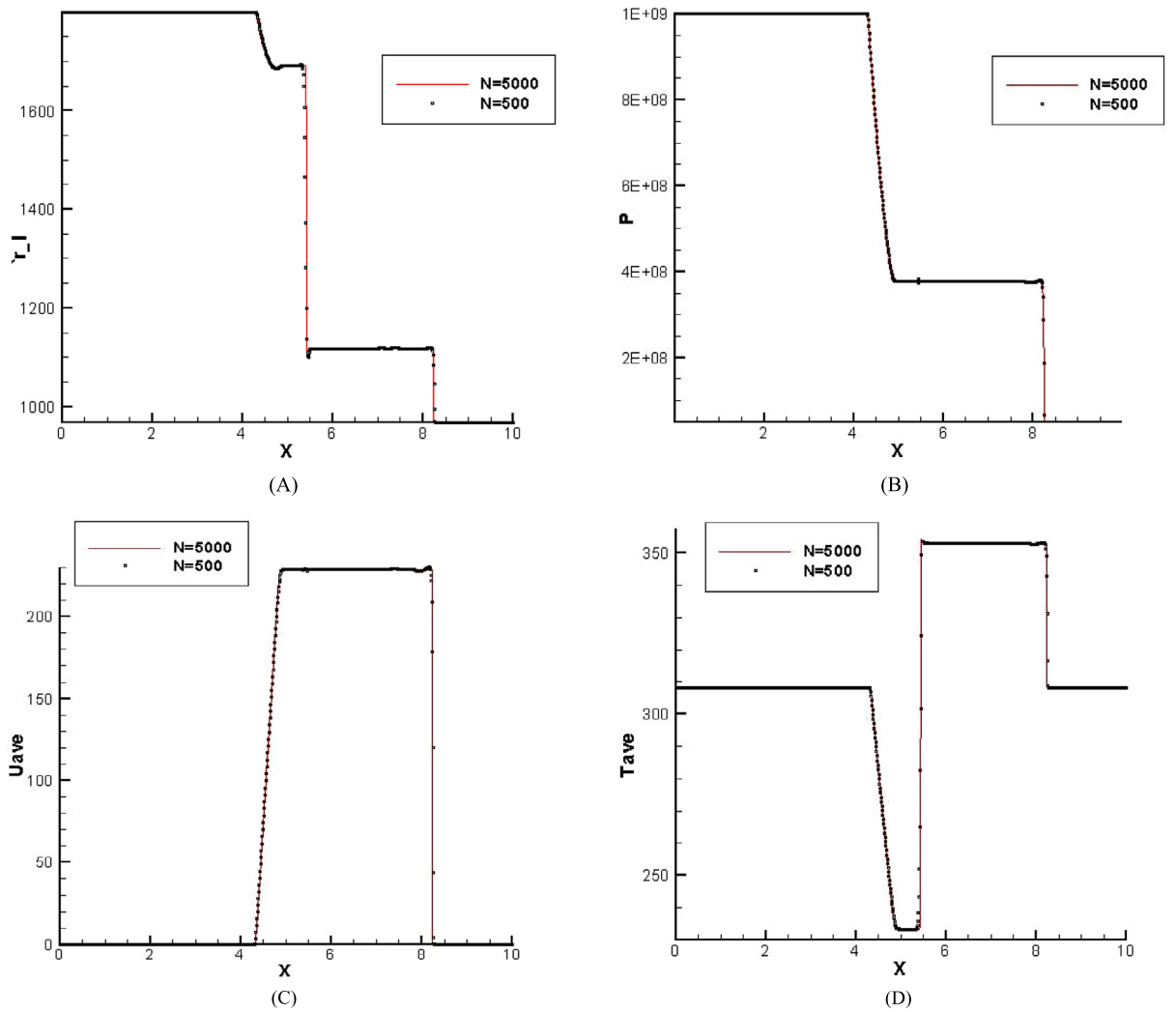

Fig. 6. Profiles of the 1D air to water shock tube problem. The initial conditions: $(p, \alpha_g, u_i, T_i)_L = (1.0 \times 10^9\ \text{Pa}, 1-\varepsilon, 0\ \text{m/s}, 308.15\ \text{K})$ $(p, \alpha_g, u_i, T_i)_R = (1.0 \times 10^5\ \text{Pa}, \varepsilon, 0\ \text{m/s}, 308.15\ \text{K})$.

Numerical applications

Ransom's faucet problem

We consider a simplified faucet flow problem proposed by Ransom [32]. As shown in Fig. 3, the water "faucet" problem consists of a liquid stream with a fixed inflow rate of water at a velocity of 10.0 (m/s), temperature of 300 K and a liquid volume fraction of 0.8 entering a vertical tube 12.0 meters in length and 1.0 meter in diameter from the top. The objective of this problem is to test numerical stability on the resolution of void propagation. Due to the action of gravity, the water falls to form a stream of uniformly decreasing cross-section. The bottom of the tube is opened to the ambient pressure. Also simple extrapolations of inflow and outflow boundary conditions are applied. Wall fraction and inter-phasic friction are not considered in this case.

As we know, Ransom's problem is a widely used benchmark test to verify the accuracy of the two fluid models and schemes. In this numerical work, a contact discontinuity moving with constant velocity and constant pressure, one necessary condition is required to capture the discontinuity exactly; especially the inter-phasic term could produce unbalanced pressure force. By doing so, the equations can be reduced to be a simple convection equation. Otherwise, the residues generated by the pressure terms will interfere with the flows and cause oscillation when the void fraction varies. Therefore, we need additional mechanism to regularize the flows, such as the interfacial pressure correction term presented in Eq. (2) as noted by Stuhmiller [5]. By increasing σ, it is noted that the void fraction profile is smeared; indicating diffusive mechanism is able to control the oscillation and regularize the flow effectively. $\sigma = 2.0$ and $CFL = 0.5$ are chosen here. In Fig. 4(A), the grid independence study is performed for the four-equation model. It is shown that the computed results on the mesh cells

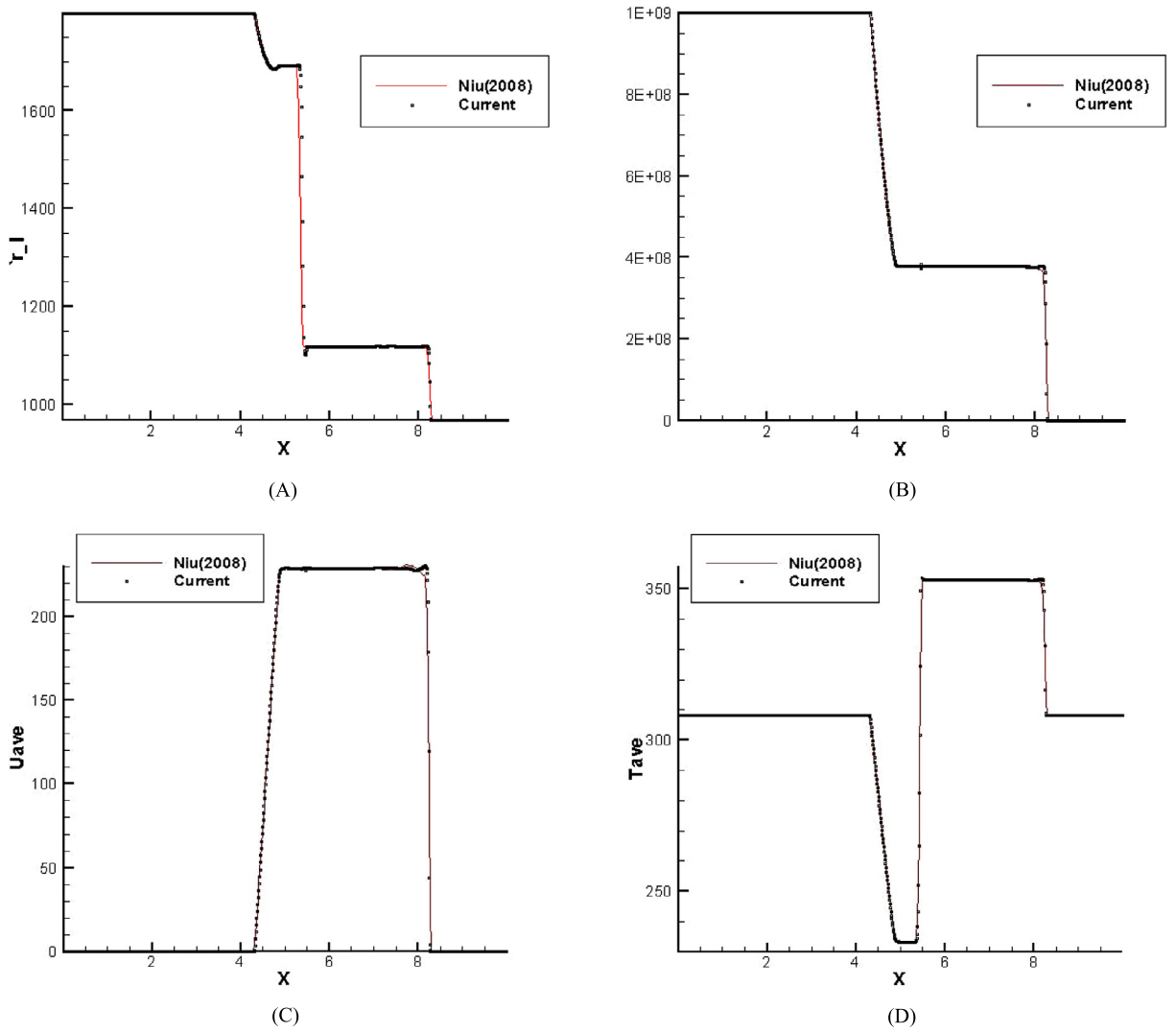

Fig. 7. Profiles of the 1D air to water shock tube problem. The initial conditions: $(p, \alpha_g, u_i, T_i)_L = (1.0 \times 10^9\ \text{Pa}, 1-\varepsilon, 0\ \text{m/s}, 308.15\ \text{K})$ $(p, \alpha_g, u_i, T_i)_R = (1.0 \times 10^5\ \text{Pa}, \varepsilon, 0\ \text{m/s}, 308.15\ \text{K})$.

of 500, 1000 and 2000 are identical. Therefore, using the 500 grid points is good enough for this case. However, the accuracy of four-equation model is not well comparable to the analytic solutions even computed on more grid points. Furthermore, in Fig. 4(B), the comparison of the computations using four- and six-equation model show that the void fraction distributions on 500 grid points done by six-equation is more accurate than four-equation model. For the six-equation model, the grid independence study is performed in Fig. 5(A). Numerical results show that using the 500 grid points is accurate as using 1000 grid points and 2000 grid points. In addition, the comparison in Fig. 5(B) of the current primitive variable Riemann solver on the resolution of void fraction distributions on 500 grid points is comparable to the previous works by AUSMD combining with exact Riemann solver. The proposed approximated Riemann solver has demonstrated its robustness in this case.

1D air to water shock tube problem

Subsequently, we consider the air–water shock tube used in the second test case as previous work [27]. The fluid states in each side of the diaphragm are defined as:

$$(p, \alpha_g, u_i, T_i)_L = \left(1.0 \times 10^9\ \text{Pa}, 1-\varepsilon, 0\ \text{m/s}, 308.15\ \text{K}\right)$$

$$(p, \alpha_g, u_i, T_i)_R = \left(1.0 \times 10^5\ \text{Pa}, \varepsilon, 0\ \text{m/s}, 308.15\ \text{K}\right)$$

A shock refraction problem describing an interface of a gas–liquid flows which is hit by the shock wave, is solved on the grids of 501 and 5001. As we know, after hitting by the incident shock wave, a shock wave transmitted across the interface

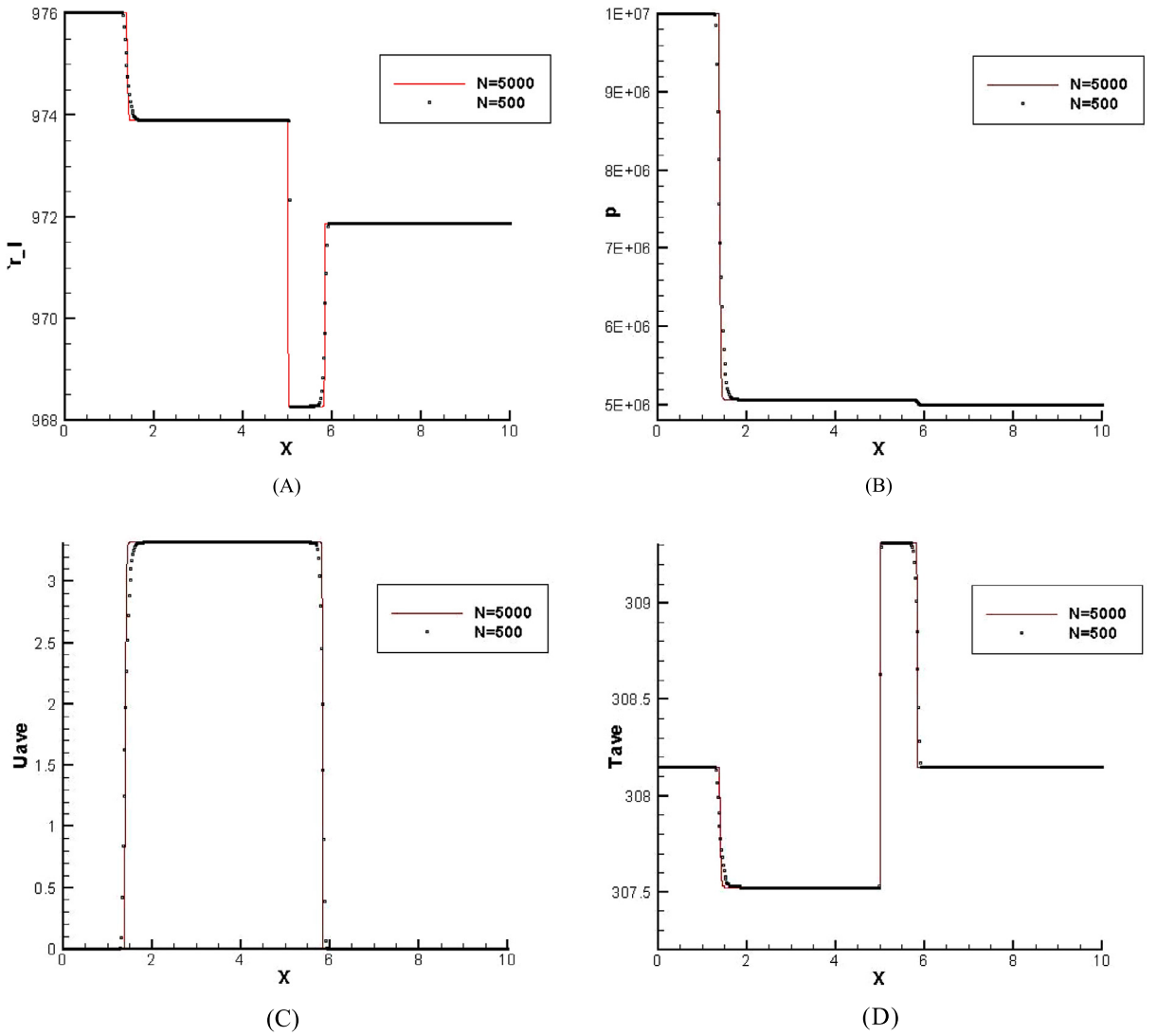

Fig. 8. Profiles of the 1D water to air shock tube problem. The initial condition: $(p, \alpha_g, u_i, T_i)_L = (1.0 \times 10^7 \text{ Pa}, \varepsilon, 0 \text{ m/s}, 308.15 \text{ K})$ $(p, \alpha_g, u_i, T_i)_R = (5.0 \times 10^6 \text{ Pa}, 1-\varepsilon, 0 \text{ m/s}, 308.15 \text{ K})$.

could become unstable physically. The simulated results are shown in Fig. 6 with $\sigma = 2.0$ and $CFL = 0.5$. The results on 501 and 5001 cells with $\varepsilon = 10^{-6}$ demonstrate that only slight oscillation can be found on the contact surfaces. Also, an identical resolution of velocities, density, pressure and temperature is visible. We observe no oscillatory behavior around all most of the results. It is encouraging to see that all of the shock waves, rarefaction waves and the fluid interfaces are sharply captured even in coarse grids of 500 points. Furthermore, in Fig. 7, it can be noted that the comparison of the current approximated Riemann solver on the resolution of the pressure, density, velocity and temperature distributions is identical to the previous works by AUSMD combining with exact Riemann solver on 500 grid points. The proposed approximated Riemann solver has also demonstrated its robustness in this case.

Next, we change the initial condition so that the shock wave propagates from the water side to the air. We have

$$(p, \alpha_g, u_i, T_i)_L = \left(1.0 \times 10^7 \text{ Pa}, \varepsilon, 0 \text{ m/s}, 308.15 \text{ K}\right)$$
$$(p, \alpha_g, u_i, T_i)_R = \left(5.0 \times 10^6 \text{ Pa}, 1-\varepsilon, 0 \text{ m/s}, 308.15 \text{ K}\right)$$

The results computed on the grids of 501 and 5001 are shown in Fig. 8 with $\varepsilon = 10^{-6}$. It is shown that the shock wave transmits from air into water due to compressibility. However, the shock wave is very difficult to travel from water into air. Only a small fraction of the shock wave is transmitted into air, and a very strong rarefaction is generated from the fluid interface and traveling back into the water. We clearly observe that the capturing of the small weak shock wave is slightly smeared in the air, however and the expansion pressure wave and contact surface are sharply captured. In addition, the liquid undergoing a strong expansion wave could be vaporized into the gas phase. The simulation of liquid density shows the

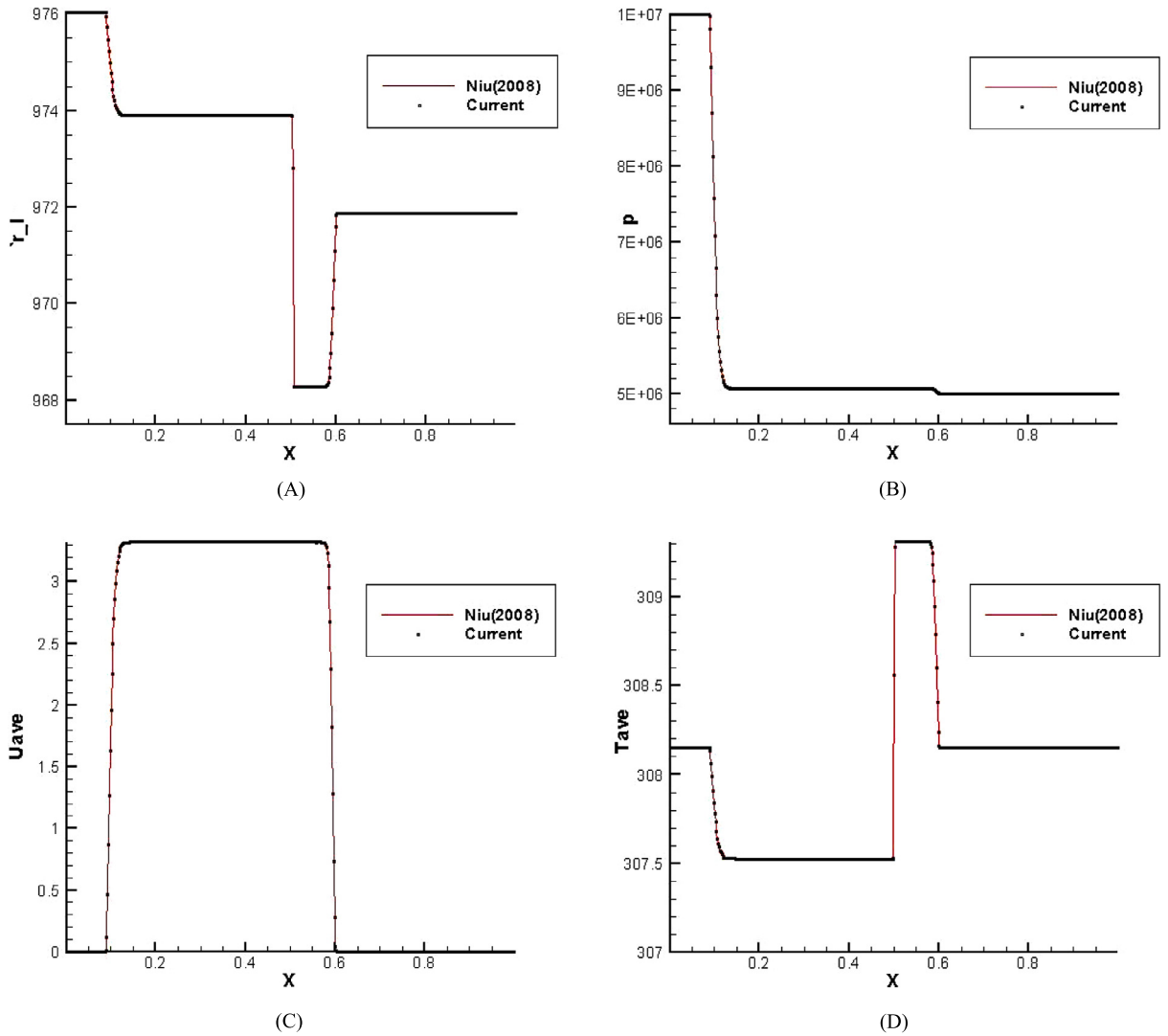

Fig. 9. Profiles of the 1D water to air shock tube problem. The initial condition: $(p, \alpha_g, u_i, T_i)_L = (1.0 \times 10^7 \text{ Pa}, \varepsilon, 0 \text{ m/s}, 308.15 \text{ K})$ $(p, \alpha_g, u_i, T_i)_R = (5.0 \times 10^6 \text{ Pa}, 1-\varepsilon, 0 \text{ m/s}, 308.15 \text{ K})$.

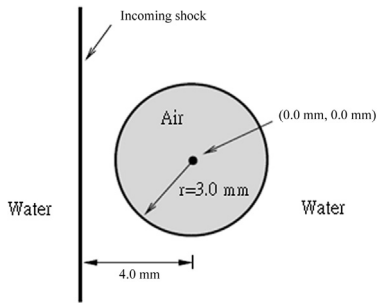

Fig. 10. Illustration of the shock–bubble interaction problem.

cavitation like behavior on the coarse and fine grids. Generally, the current approximated Riemann solver on coarse is shown to capture shock and rarefaction wave both in air and water flows very well. Accurate and consistent results are presented based on grid independence study. Furthermore, Fig. 9 demonstrates that the comparison of the current approximated Riemann solver on the resolution of liquid density, pressure, mixture velocity and mixture temperature distributions on 500

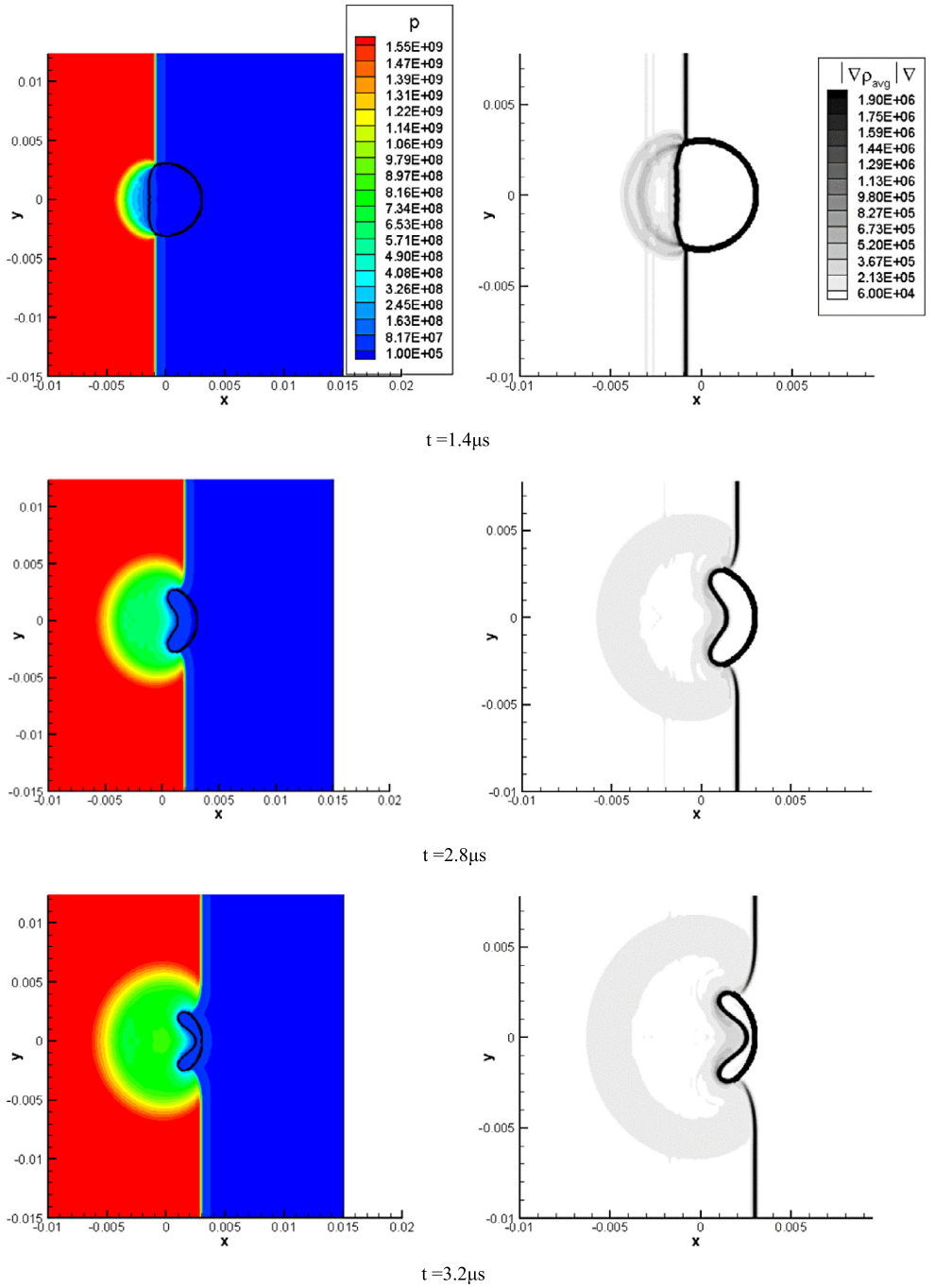

Fig. 11. Time evolution of the shock–bubble interaction problem. Left: contours of pressure; Right: void fraction contours $(1+\alpha_g^2)\log(|\nabla\rho_{avg}|+1)$ (numerical schlieren).

grid points is identical to the previous works by AUSMDV combining with exact Riemann solver. The robustness of the proposed approximated Riemann solver is further verified.

Results of 2D shock–bubble interaction problem

In the third case, the interaction of underwater shock and the air bubble is simulated. We have to note that the current benchmark test cannot be done in our previous studies based on pure AUSMDV if without combing with exact Riemann solver. The initial condition used by [29] is adopted. The air bubble with diameter 6.0 mm is immersed in the water pool

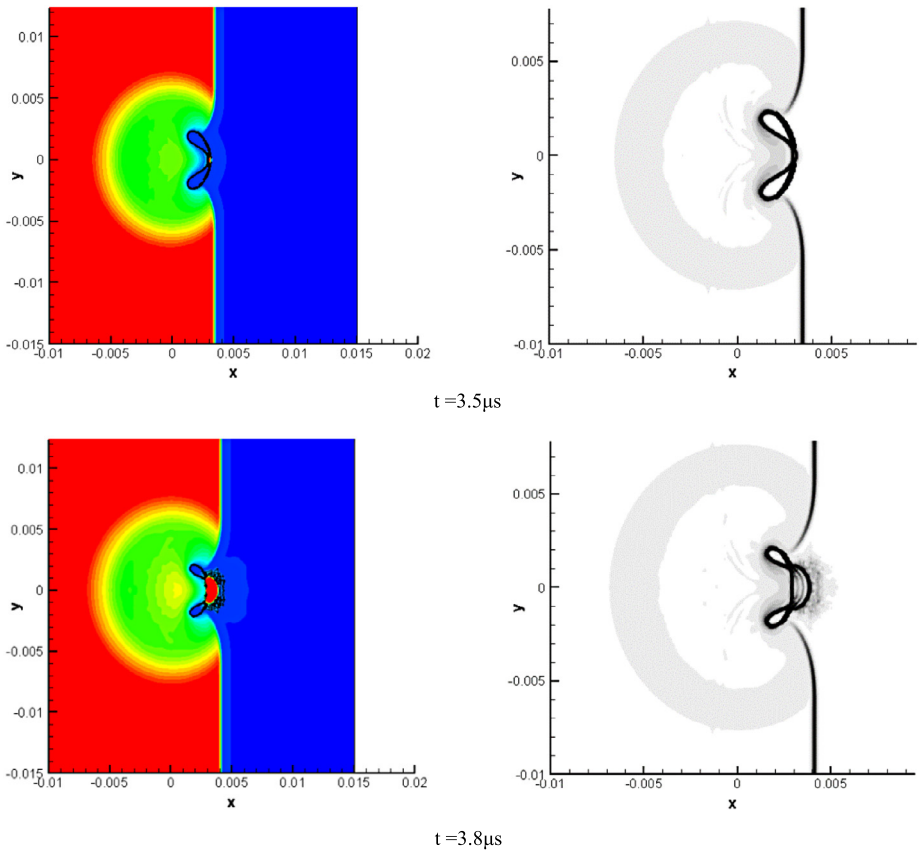

Fig. 11. (*continued*)

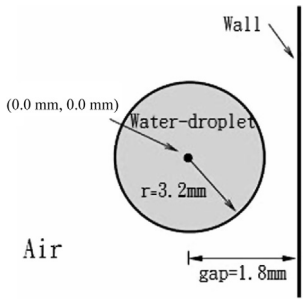

Fig. 12. The water droplet impact problem.

with its center in the origin. The incoming shock is initially located in $x = -4.0$ mm. The initial condition is shown in Fig. 10. The fluid states before the shock is

$$p = 1.013250 \times 10^5 \text{ Pa}, \qquad u_i = v_i = 0 \text{ m/s}, \qquad T_i = 292.98 \text{ K}$$

and the states behind of the shock are:

$$p = 1.6 \times 10^9 \text{ Pa}, \qquad u_i = 661.81 \text{ m/s}, \qquad v_i = 0 \text{ m/s}, \qquad T_i = 595.14 \text{ K}$$

The time evolution of the simulated evolutions of the pressure and numerical schlieren is presented in Fig. 8. It is clear seen that the interface of the gas droplet is getting curved when water shock wave hits the bubble, then a strong reflection rarefaction wave is developed and rebounding during the times changes from $t = 1.4$–3.5 μs as shown in Fig. 11. A water jet generated by the rarefaction wave continuously pushes the bubble into a crescent shape until the bubble begins to separate into the two halves. When the bubble finally breakups, the water jet velocity is increased between the two halves of the bubble after the time equals 3.5 μs, also coming with high pressure producing in between. The shock collision with the gas bubble generates several rebounding shock waves propagating radially around the two separated bubbles. Meanwhile,

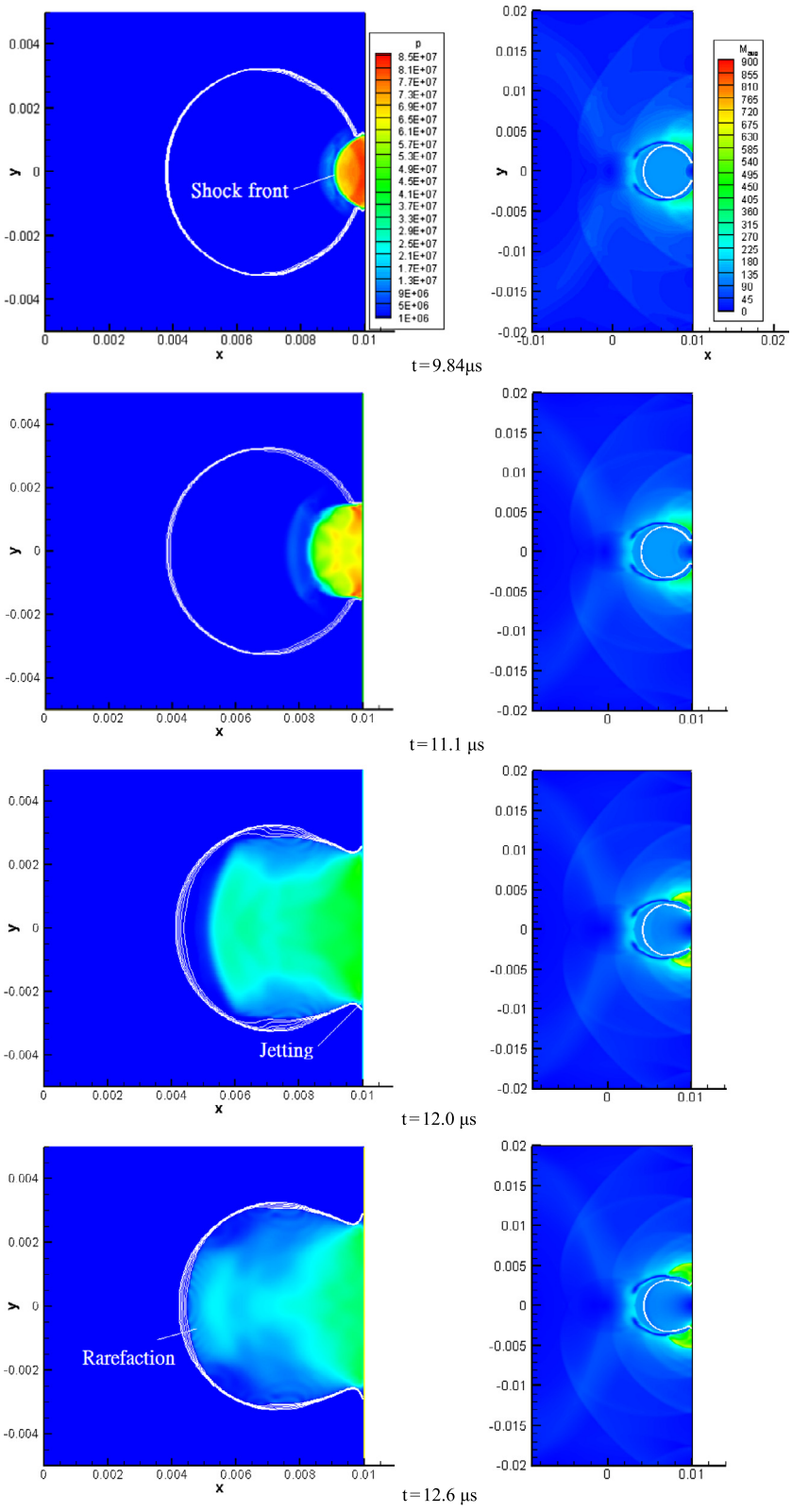

Fig. 13. The water droplet interaction with wall problem ($V = 134$ m/s). Left: contours of pressure in enlarged domain; Right: velocity contours.

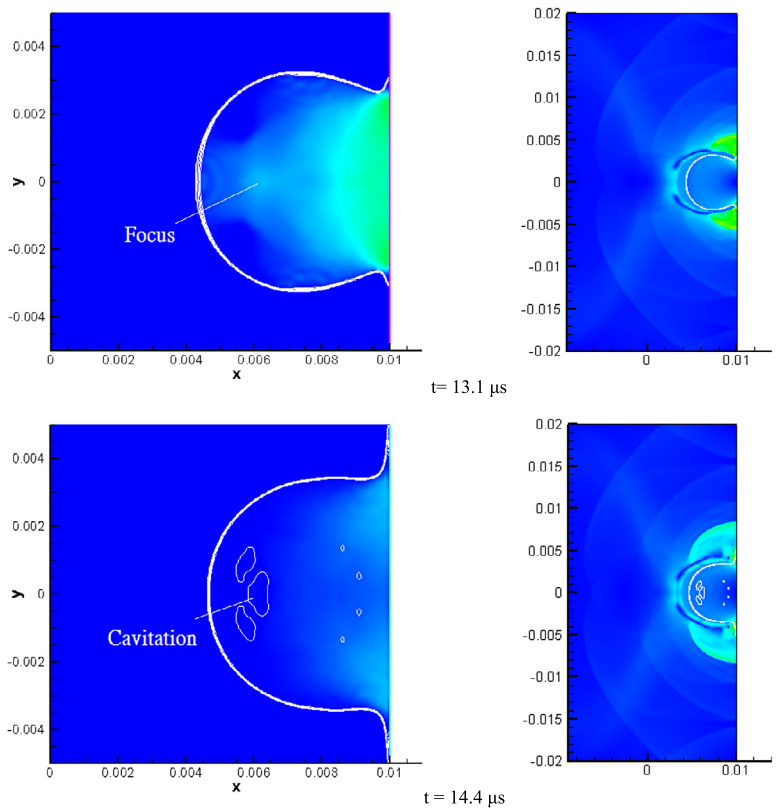

Fig. 13. (*continued*)

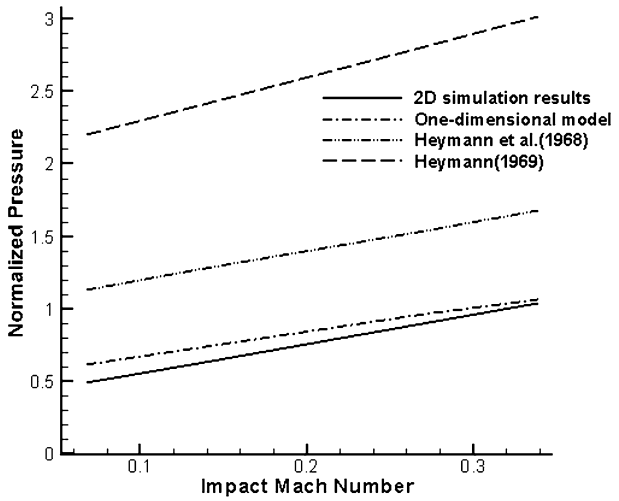

Fig. 14. Comparison of normalized wall pressure versus different impact Mach numbers done by different approaches (one-dimensional model is the so-called surface elastic theory noted in [35]).

the separated air bubbles are compressed into very small volume due to the increasing high pressures opposed on it ($t = 3.8$–5.0 μs). A strong increasing high pressure is also produced towards the wall. In addition, the evolution of sharp interfaces is captured by the current scheme and model without unwanted oscillative errors.

Results of liquid droplet impact on walls

In the final case [22,34,35], the gas and liquid fluid are governed by the perfect gas model and stiffened gas model, respectively. Two-dimensional single droplet impingement on a wall is analyzed; the initial conditions and computed diagram

are shown in Fig. 12. The surrounding of the droplet is assumed as the air, we examined the impact of a single water droplet of a 3.2 mm radius moving with an initial velocity of 134, 200 and 500 m/s towards a solid surface, the distance between droplet and wall is 1.8 mm. In our calculations, the high Reynolds number above 500,000 implies inertia dominated the phenomena and supports an inviscid approach to the problem. The Weber number around 1,800,000 is supporting that the surface tension effect is neglected. Therefore, the slip condition is used to deal with the solid wall conditions when the droplet hits the wall instead of complicated contact line conditions. The initial gas flow conditions we chose are

$$p = 1.013250 \times 10^5 \text{ Pa}, \qquad u_i = v_i = 0 \text{ m/s}, \qquad T_i = 300 \text{ K}$$

and the states of the liquid droplet are:

$$p = 1.1 \times 10^5 \text{ Pa}, \qquad u_i = 200 \text{ m/s}, \qquad v_i = 0 \text{ m/s}, \qquad T_i = 300 \text{ K}$$

Computational investigation only shows that the impact of a high velocity of 134 m/s droplet on a rigid wall. The time evolution of the simulation is presented in Fig. 13. We observe that the pressure evolution in the symmetry plane of the droplet during the impingement. Initially, the water droplet has the ambient pressure around and inside itself. Immediately upon impact, we can observe the creation of a strong shock wave begins at the first moment of impact on the wall, and then moves upward. It has been demonstrated that compressible flow patterns dominate the early droplet impact process and splashing during the past works. The simulations show that upon collision, a shock wave attached to the contact edge of the droplet is generated. The liquid zone adjacent to the surface is highly compressed and bounded by the shock envelope, which separates it from the unaffected bulk of the liquid. Subsequently, the pressure difference across the free surface at the contact edge region triggers the eruption of intense lateral jetting of high velocity. The shock wave travels along the free surface of the droplet and is reflected into the bulk of the liquid as an expansion wave. Thus, the shock wave remains attached to the contact periphery up to the time 9.84 μs. After this time the shock wave overtakes the contact line, starting to travel along the droplet free surface. At the free surface, the shock wave is reflected normal to the surface as an expansion wave, which focuses in the inner region of water droplet. The shock wave propagating upward finally reaches the droplet upmost point where it is reflected downward. As the shock wave travels along the free surface, it carries a low pressure area ultimately focusing at the droplet axis of symmetry during $t = 12.6$–13.1 μs. The presence of low pressure, indicating strong rarefaction in the middle of the drop, could produce cavitation like regions around the area in which rarefaction wave rebounding to the focus point obviously at $t = 14.4$ μs. The sequence of plots demonstrates numerically that high-velocity droplet impact is dominated by compressibility done by the two-fluid model, with the development of lateral jetting and the generation of shock and expansion waves. In addition, the grid independence study is performed. The evolution of the phenomena inside the droplet and maximum pressure on walls are not shown in the large disparity. To compare with the previous works [22,34,35], our predicted wall pressure under different impact velocities computed by the current six-equation model is much closer to the theoretical one-dimensional model [35] than any other model which can be clearly seen from Fig. 14.

Conclusions and suggestions

In this work, a hybrid Primitive Variable Riemann solver (PVRS) with AUSMD is proposed to simulate multi-phase flows described by a four- and a six-equation two-fluid model with the stiffened equation of state. The proposed scheme has been demonstrated accurate capturing of the liquid pressure waves and the interfaces of the complicated shock–bubble dynamics flows in the benchmark cases. In addition, the proposed scheme can achieve the stable simulation of the interfaces between the liquid–liquid, gas–liquid and gas–gas concurrently, also it is very simple to implement with less computer time consuming. The proposed hybrid type linearized Riemann solver indicates great potential of solving further complicated multi-fluid problems.

Acknowledgements

The author acknowledges the support of Ministry of Science and Technology, R.O.C. under the grant of 103-2221-E-032-024-MY3, also fruitful discussions on the AUSM type scheme with Dr. M.S. Liou from NASA John H. Glenn Research Center, USA and the two-fluid model with Dr. C.H. Chang at Theofanous Co., CA, USA.

References

[1] M. Ishii, Thermo-Fluid Dynamic Theory of Two-Phase Flow, Eyrolles, Paris, 1975.
[2] H.B. Stewart, B. Wendroff, Review article; two-phase flow: models and methods, J. Comput. Phys. 56 (1984) 363–409.
[3] D. Drew, L. Cheng, R.T. Lahey, The analysis of virtual mass effects in two-phase flow, Int. J. Multiph. Flow 5 (1979) 233–242.
[4] D.A. Drew, S.L. Passman, Theory of Multicomponent Fluids, Appl. Math. Sci., vol. 135, Springer-Verlag, New York, 1999.
[5] J.H. Stuhmiller, The influence of interfacial pressure forces on the character of two-phase flow model equations, Int. J. Multiph. Flow 3 (1997) 551–560.
[6] D. Bestion, The physical closure laws in the CATHARE code, Nucl. Eng. Des. 124 (1990) 229–245.
[7] I. Toumi, A. Kumbaro, An approximate linearized Riemann solver for two-fluid model, J. Comput. Phys. 124 (1996) 286–300.
[8] M.R. Baer, J.W. Nunziato, A two-phase mixture theory for the deflagration-to-detonation transition (DDT) in reactive granular materials, Int. J. Multiph. Flow 12 (1986) 861–889.

[9] R. Saurel, R. Abgrall, A multiphase Godunov method for compressible multi-fluid and multiphase flows, J. Comput. Phys. 150 (1999) 425–467.
[10] Y.-Y. Niu, Numerical approximations of a compressible two fluid model by the advection upwind splitting method, Int. J. Numer. Methods Fluids 36 (2001) 351–371.
[11] G. Allaire, S. Clerc, S. Kokh, A five-equation model for the simulation of interface between compressible fluids, J. Comput. Phys. 181 (2002) 577–616.
[12] A. Murrone, H. Guillard, A five equation reduced model for compressible two phase flow problems, J. Comput. Phys. 202 (2005) 664–698.
[13] A.K. Kapila, S.F. Son, J.B. Bdzil, R. Menikoff, D.S. Stewart, Two-phase modeling of DDT: structure of the velocity-relaxation zone, Phys. Fluids 9 (12) (1997) 3885–3897.
[14] J.J. Kreeft, B. Koren, A new formulation of Kapila's five-equation model for compressible two-fluid flow, and its numerical treatment, J. Comput. Phys. 229 (2010) 6220–6242.
[15] K.M. Shyue, F. Xiao, An Eulerian interface sharpening algorithm for compressible two-phase flow: the algebraic THINC approach, J. Comput. Phys. 258 (2014) 95–117.
[16] J. Glimm, X. Li, Y. Liu, Z. Xu, Z. Zhao, Conservative front tracking with improved accuracy, SIAM J. Numer. Anal. 39 (2003) 179–200.
[17] B. Hu, N.A. Khoo, F. Huang, A conservative interface method for compressible flows, J. Comput. Phys. 219 (2006) 553–578.
[18] M. Sussman, P. Smereka, S. Osher, A level set approach for computing solutions of incompressible two-phase flows, J. Comput. Phys. 114 (1994) 146–159.
[19] W. Hirt, B.D. Nichols, Volume of fluid method for the dynamics of free boundaries, J. Comput. Phys. 39 (1981) 201–225.
[20] E.F. Toro, M. Spruce, W. Speares, Restoration of the contact surface in the HLL-Riemann solver, Shock Waves 4 (1994) 25–34.
[21] S.A. Tokareva, E.F. Toro, HLLC-type Riemann solver for the Baer–Nunziato equations of compressible two-phase flow, J. Comput. Phys. 229 (2010) 3573–3604.
[22] T. Sanada, K. Ando, T. Colonius, A computational study of high-speed droplet impact, Fluid Dyn. Mater. Proc. 7 (4) (2011) 329–340.
[23] M.-S. Liou, A sequel to AUSM: AUSM$^+$, J. Comput. Phys. 129 (1996) 364–382.
[24] Y. Wada, M.-S. Liou, An accurate and robust flux splitting scheme for shock and contact discontinuities, SIAM J. Sci. Comput. 18 (3) (1997) 633–657.
[25] C.-W. Su, S. Osher, Efficient implementation of essentially non-oscillatory shock-capturing schemes, J. Comput. Phys. 77 (1988) 439–471.
[26] E.F. Toro, Riemann Solvers and Numerical Methods for Fluid Dynamics: A Practical Introduction, 2nd ed., Springer-Verlag, 1999.
[27] H. Paillère, C. Corre, J.R. García Cascales, On the extension of the AUSM$^+$ scheme to compressible two-fluid models, Comput. Fluids 32 (2003) 891–916.
[28] J.R. Edwards, R.K. Franklin, M.-S. Liou, Low-diffusion flux-splitting methods for real fluid flows with phase transitions, AIAA J. 38 (2000) 1624–1633.
[29] C.-H. Chang, M.-S. Liou, A new approach to the simulation of compressible multifluid flows with AUSM$^+$-up scheme, J. Comput. Phys. 225 (2007) 840–873.
[30] M.-S. Liou, C.-H. Chang, L. Nguyen, T.G. Theofanous, How to solve compressible multifluid equations: a simple, robust, and accurate method, AIAA J. 46 (2008) 2345–2356.
[31] Y.-Y. Niu, Y.-C. Lin, C.-H. Chang, A further work on multi-phase two-fluid approach for compressible multi-phase flows, Int. J. Numer. Methods Fluids 58 (2008) 879–896.
[32] V.H. Ransom, Numerical benchmark tests, in: G.F. Hewitt, J.M. Delhaye, N. Zuber (Eds.), Multiphase Science and Technology, vol. 3, Hemishpere Publishing Corporation, 1987.
[33] B. Van Leer, Towards the ultimate conservative difference scheme. V. A second-order Sequel to Godunov's method, J. Comput. Phys. 32 (1979) 101–136.
[34] K. Haller, Y. Ventikos, D. Poulikakos, P. Monkewitz, Computational study of high-speed liquid droplet impact, J. Appl. Phys. 92 (2002) 2821.
[35] F.J. Heymann, High-speed impact between a liquid drop and a solid surface, J. Appl. Phys. 40 (13) (1969) 5113–5122.
[36] E. Romensky, A.D. Resnyanski, E.F. Toro, Conservative hyperbolic formulation for compressible two-phase flow with different phase pressures and temperatures, Q. Appl. Math. 6 (2007) 259–279.
[37] Michael Dumbser, Manuel Castro, Carlos Pares, Eleuterio Toro, Arturo Hidalgo, FORCE schemes on unstructured meshes II: non-conservative hyperbolic systems, Comput. Methods Appl. Mech. Eng. 199 (9–12) (2010) 625–647.